

Dynamic Inchworm Crawling: Performance Analysis and Optimization of a Three-link Robot

Benny Gamus, Amir D. Gat, and Yizhar Or

Abstract—Inchworm crawling allows for both quasistatic and dynamic gaits at a wide range of actuation frequencies. This locomotion mechanism is common in nonskeletal animals and exploited extensively in the bio-inspired field of soft robotics. In this work we develop and simulate the hybrid dynamic crawling of a three-link robot, with passive frictional contacts. We fabricate and experimentally test such robot under periodic inputs of joints' angles, with good agreement to the theoretical predictions. This allows to comprehend and exploit the effects of inertia in order to find optimal performance in inputs' parameters. A simple criterion of robustness to uncertainties in friction is proposed. Tuning the inputs according to this criterion improves the robustness of low-frequency actuation, while increasing the frequency allows for gaits with both high advancement velocity and robustness. Finally, the advantages of uneven mass distribution are studied. Time-scaling technique is introduced to shape inputs that achieve similar effect without reassembling the robot. A machine-learning based optimization is applied to these inputs to further improve the robot's performance in traveling distance.

I. INTRODUCTION

In mobile robots, legged locomotion is advantageous in negotiating unstructured terrains, where wheeled and tracked vehicles have limited maneuverability or accessibility [1]. Bipedal legged robots are also widely studied due to their resemblance to humans and other mammals. Though this robotic configuration has relatively low dimensionality, it usually performs complicated *dynamic* locomotion, where the robot constantly undergoes unsteady motion of falling, followed by the replacement of the support foot in a cyclic pattern (*gait*).

Inchworm crawling is a type of legged locomotion which is characterized by multiple persistent ground contacts, which alternate stick-slip transitions. This allows for crawling gaits to be possible at a wide range of actuation frequencies. For rapid actuation, when the inertial effects are not negligible, dynamic inchworm crawling occurs (which will be the focus of this study). However, for slow actuation, the same locomotion mechanism also allows to remain in static balance while performing *quasistatic* movement – i.e. transitioning within a continuum of static equilibria – even on two contacts. Probably for that reason crawling is common in many nonskeletal

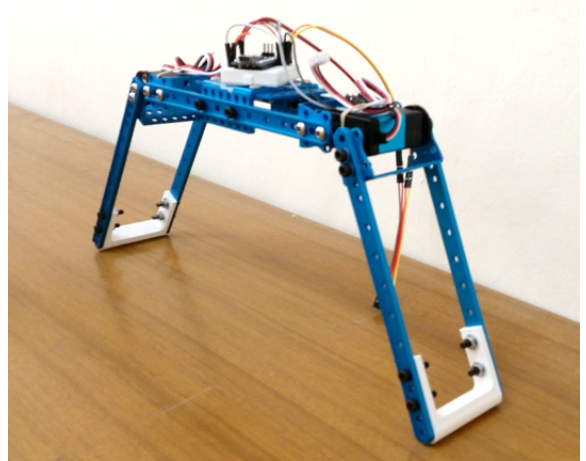


Fig. 1: Our three-link robot experimental prototype

animals, such as worms and caterpillars, octopi and crawling cells. Most of these creatures generate motion by manipulating fluids in their bodies [2] – which is a rather slow process, compared to skeletal animals with rapidly contracting muscles.

The actual inchworm, crawling cells and some crawling robots actively manipulate the contact interaction by adhesion [3], [4]. Many crawling robots utilize directional friction [5]–[8], which do not allow to reverse the movement direction, while others perform crawling with passive frictional contacts [9], [10]. The latter, which will be the focus of this study, is a more complicated yet more general approach.

In recent years, crawling is exploited extensively [11] in the rapidly growing bio-inspired field of *soft robotics* [12]. In these robots, which draw inspiration from nonskeletal animals, actuation is often similarly created by pressurizing fluids in internal cavities of their compliant structure. Nonetheless, rapid dynamic movement of soft robots can also be achieved – with other actuation methods, such as magnetic fields [13].

In previous works [14] we have shown that a three-link model (Fig. 2) captures well the major phenomena of quasistatic inchworm crawling of a soft bipedal robot. This lumped model is a very basic form of multi-contact bipedal crawling, in analogy to McGeer's biped [15] being a benchmark of bipedal walking. Yet, most “traditional” articulated legged robots are of higher complexity and often have more legs [16], [17]. To the best of our knowledge, the minimal three-link robot has not been noticeably studied.

The purpose of this study is to model and analyze the dynamic bipedal frictional inchworm crawling locomotion, in order to comprehend and exploit the effects of inertia, for both

We thank Mr. Yinon Graitzer and Mr. Shay Tovy for constructing the robot and Ms. Bat-Chen Hozé for conducting the experiments. This work was supported by Israel Science Foundation under grant no. 1005/19, Israel Ministry of Science and Technology under grants number 3-14418 and 3-15622, and Technion's Center for Security Science and Technology (CSST) under grant no. 2027795.

Benny Gamus, Amir D. Gat and Yizhar Or are with the Faculty of Mechanical Engineering, Technion – Israel Institute of Technology, Technion City, Haifa, Israel 3200003.

soft and articulated robots. First, we develop a model for the hybrid dynamic [18] crawling (i.e. with discrete transitions between contact states) of a three-link robot with passive frictional contacts. The robot is actuated in open-loop by prescribing periodic inputs to its joints' angles. We study the effects of frequency and other input parameters on the crawling gait, and find trends and optimal performance. We manufacture and experimentally test a three-link robot (Fig. 1) with good quantitative and excellent qualitative agreement with the theoretical predictions, which proves the applicability of our analysis (see supplementary video [19]). We also investigate the effects of friction uncertainties, which was shown to have major influence [20], and mass asymmetry, propose a novel input shaping technique and apply machine-learning based optimization to improve the performance in traveling distance. Finally, we discuss a feedback control strategy.

II. PROBLEM FORMULATION

In order to investigate crawling at frequency range where inertial effects are significant, we have manufactured the three-link robot prototype in Fig. 1. The robot has a central link with length l_0 , mass m_0 and moment of inertia J_0 and two distal links, with length l_i , mass m_i and moment of inertia J_i , for $i = 1, 2$ (see Fig. 2). For most of this work we consider identical distal links $l_1 = l_2 \equiv l$, $m_1 = m_2 \equiv m$, $J_1 = J_2 \equiv J$, and in Section VII we investigate the influence of asymmetric mass distribution. The experimental setup parameters are summarized in Table I. Two servomotors at the joints receive a sequence of angle commands from the microcontroller (in open-loop) and track it with internal closed-loop control.

Assuming planar motion and point-contacts, a corresponding three-link model is proposed in Fig. 2. The motion of the robot can be described by the generalized coordinates $\mathbf{q}(t) = [x \ y \ \theta \ \varphi_1 \ \varphi_2]^T$, where (x, y, θ) are the planar position and absolute orientation angle of the central link, and (φ_1, φ_2) are the joint angles. Throughout this work we assume that the two joint angles $\mathbf{q}_c(t) = [\varphi_1(t) \ \varphi_2(t)]^T$ are prescribed directly as known periodic input functions (and hence their time-derivatives $\dot{\mathbf{q}}_c(t)$, $\ddot{\mathbf{q}}_c(t)$ are also known). This assumption, which is quite reasonable for a robot with joints controlled in closed-loop, significantly simplifies the analysis by effectively reducing the number of dynamically-evolving degrees-of-freedom (DoF).

A closed-chain four-bar mechanism has only one DoF. Hence, for general prescribed two joint angles $\mathbf{q}_c(t)$, at least one of the contacts is always constrained to slip (except for discrete times, where the relative velocity between feet vanishes). Therefore, there are only three possible combinations of the contacts' states – stick-slip, slip-stick and slip-slip – which we now turn to model.

III. HYBRID DYNAMIC MODEL

In this section we introduce the derivation of a hybrid dynamic model which accounts for the different contact states of our three-link robot.

Denoting the position vectors of the contacts as $\mathbf{r}_i = [x_i \ y_i]^T$ (for $i = 1, 2$), the velocities of the i -th contact are

$$\mathbf{v}_i = \dot{\mathbf{r}}_i = \mathbf{W}_i(\mathbf{q})\dot{\mathbf{q}}, \quad (1)$$

with the Jacobian matrices

$$\mathbf{W}_i(\mathbf{q}) = \frac{\partial \mathbf{r}_i(\mathbf{q})}{\partial \mathbf{q}^T}. \quad (2)$$

The dynamic motion equations can be written in a standard matrix form [21]

$$\mathbf{M}(\mathbf{q})\ddot{\mathbf{q}} + \mathbf{B}(\mathbf{q}, \dot{\mathbf{q}}) + \mathbf{G}(\mathbf{q}) = \mathbf{E}\boldsymbol{\tau}(t) + \mathbf{W}(\mathbf{q})^T \mathbf{F}(t), \quad (3)$$

where the terms of the matrices \mathbf{M} , \mathbf{B} , \mathbf{G} , \mathbf{E} and the Jacobian $\mathbf{W} = [\mathbf{W}_1^T \ \mathbf{W}_2^T]^T$ are given in the Appendix, and $\boldsymbol{\tau}(t) = [\tau_1(t) \ \tau_2(t)]^T$ are the internal input torques at the joints. The term $\mathbf{F}(t) = [f_1^x \ f_1^y \ f_2^x \ f_2^y]^T$ is the vector of generalized constraint forces, acting at the i -th contact in the normal (superscript y) and tangential (superscript x) directions (via the Jacobian \mathbf{W}). The contact forces vary with the different locomotion modes as we introduce next.

Though the constrained coordinates $\mathbf{q}_c(t)$ (and their time-derivatives) are known, we are still left with three unconstrained body coordinates $\mathbf{q}_b(t) = [x \ y \ \theta]^T$, two actuation torques $\boldsymbol{\tau}(t)$ and four contact forces $\mathbf{F}(t)$. This gives 9 unknowns with 5 motion equations (3), hence the motion is governed by additional constraints, as introduced next.

In inchworm crawling, the legs maintain persistent contact with the ground, giving two kinematic constraints $y_1 = y_2 = 0$ (these assumptions are constantly verified by calculating the normal forces at the contacts and requiring $f_i^y > 0$). If one of the legs is in contact-sticking (stick-slip or slip-stick modes) we also get a third constraint $\dot{x}_i = 0$ for the sticking contact, yet additional constitutive relations are required. Coulomb's dry friction model dictates that the tangential forces f_i^x must maintain

$$|f_i^x| \leq \mu f_i^y \quad - \text{for a sticking contact} \quad (4a)$$

and

$$f_i^x = -\mu f_i^y \text{ sign } \dot{x}_i, \quad - \text{for a slipping contact}, \quad (4b)$$

where μ is Coulomb's friction coefficient (for simplicity, we do not distinguish between static and kinetic friction coefficients). Thus the overall count gives 9 unknowns with 5 equations of motion, two constraints in the normal direction, and two tangential constraints – either $\dot{x}_i = 0$ for a sticking contact or (4b) for slippage. This system is complete and allows for a closed solution.

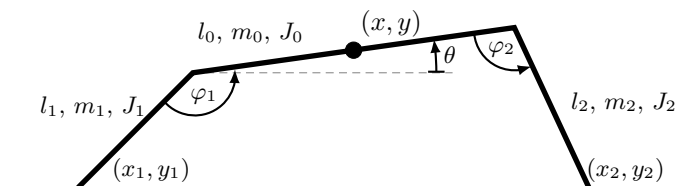


Fig. 2: Three-link robot model

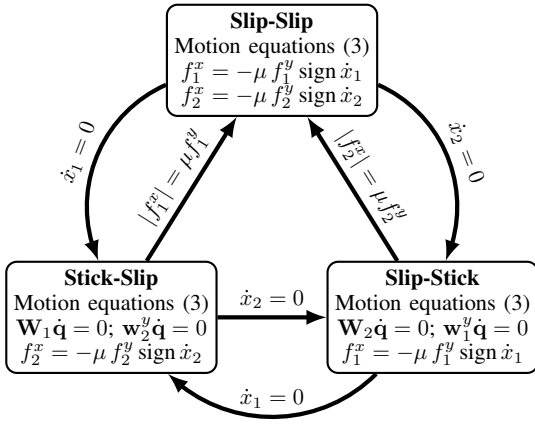


Fig. 3: Transition graph of contacts states

We can now decompose matrices \mathbf{M} and \mathbf{W} into blocks corresponding to the constrained and unconstrained coordinates, and rearrange (3) and the constraints (using (1)) such that all the unknowns are on one side of the equation (see Appendix for details). These motion equations can be solved simultaneously with the constraints for each contact state with a numerical solver (for our simulation we are using MATLAB® ode45 with event detection).

The conditions for transitions between contact states are as follows. A contact remains in slippage as long as its tangential velocity $\dot{x}_i \neq 0$. When $\dot{x}_i = 0$, the contact either turns to contact-sticking, or reverses slippage direction. Contact-sticking may only hold as long as the tangential friction force satisfies (4a), otherwise slippage occurs. The simulation detects such crossings and switches accordingly the constraints we solve for. Fig. 3 depicts a transition graph of all the contact states.

IV. ANALYSIS AND RESULTS

In this section we investigate the influence of various parameters on the robot’s performance via the numerical simulation. Then, in Section V, these results are compared to experiments (also see supplementary video [19]). We choose concrete periodic functions of the angles as follows

$$\varphi_1(t) = \varphi_0 + A \sin(\omega t + \psi/2), \quad (5a)$$

$$\varphi_2(t) = \varphi_0 + A \sin(\omega t - \psi/2), \quad (5b)$$

where φ_0 is the nominal angle, A is the oscillation amplitude, ψ is the phase difference between the legs, and ω is the frequency. The performance is measured via the net distance traveled per step (in steady state) $S \equiv x_1(t) - x_1(t - T)$ and the average step velocity $V \equiv S/T$, where $T \equiv 2\pi/\omega$ is the period time.

Parametric investigation of the simulation shows some influence and coupling of all the parameters. The most significant effects are achieved by varying the actuation frequency ω , as shown in Fig. 4 (solid blue curves) for $A = 18^\circ$, $\varphi_0 = 110^\circ$ and $\psi = 20^\circ$. To further comprehend these results we divide the frequencies into three ranges (marked by ① to ③ in

Fig. 4) and plot in Fig. 5 the contacts’ velocities $\dot{x}_i(t)$ for one representative frequency in each range. These selected frequencies are also indicated by arrows in Fig. 4(b). In the low frequencies (range ①), the inertial effects are minor and the robot performs gaits with almost ideal switching – where the contacts slip consecutively only in the desired advancement direction. This is illustrated by the contacts’ velocities $\dot{x}_i(t)$ in Fig. 5(a) (dashed curves), and corresponds to results achieved with quasistatic analysis in [14]. In this frequency range, since the distance S is almost steady but the cycle time shortens as $1/\omega$, the average velocity V increases with frequency (see Fig. 4(b)). In range ②, as the frequency increases, a growing portion of the cycle exhibits slippage in the opposing direction, until the advancement is almost entirely canceled. The velocities $\dot{x}_i(t)$ at a frequency with minimal advancement are depicted in Fig. 5(b). In this range, S shortens faster than the cycle time T , and the average velocity decreases. Finally, for even higher frequencies (in range ③), though the robot continues to exhibit opposing slippage throughout the cycle, it also develops a rigid-body progression in the desired direction. This increases the net distance only slightly, but since the frequency is in a high range the average velocity rises rapidly. In Fig. 5(c) we notice that for a short portion of the cycle both contacts have positive slippage velocities $\dot{x}_i > 0$.

We can also find *optimal phase difference* ψ^* which maximizes the distance S for each frequency. The optimum $\psi^*(\omega)$ shifts (almost monotonically in ω) from $\psi^* \rightarrow 0$ for low frequencies (with agreement to the quasistatic limit in [14]) towards $\psi^* \approx 120^\circ$ as the frequency rises. This is depicted by the dotted black curve over the $\psi - \omega$ parametric space in Fig. 6. Moving average is applied to the curve in order to reduce numerical noise, especially for the frequency range where S is small.

Another interesting effect of inertia is observed with a variation of the nominal angle. At large enough φ_0 (i.e. “flatter” robot), by varying the input frequency ω a *direction reversal* occurs, as shown in Fig. 7(a) in solid blue curve (for $\varphi_0 = 145^\circ$, $A = 18^\circ$ and $\psi = 20^\circ$). The same phenomenon is observed for a sweep of the nominal angle φ_0 at a frequency in the above range ($\omega = 9$ [rad/s]) in Fig. 7(b).

V. EXPERIMENTS

In order to measure the performance of our robot in Fig. 1, we video it with a simple webcam. The video lens distortion is then corrected with MATLAB® Computer Vision System Toolbox and post-processed with Kinovea software, which gives planar x-y position of selected points on the robot’s links. Since the robot is controlled in open-loop, as the frequency increases the servo struggles to follow the prescribed amplitude. Therefore we initially calibrate the amplitudes of inputs’ reference trajectories to achieve the desired angles in (5), and validate the other parameters (such as frequency).

In an additional preliminary calibration experiment, we measure the friction coefficient by tilting the plane with the robot rigidly standing on top, and finding (with image processing) the angle at which the robot starts to slip (see Table. I).

At each set of parameters the robot performs five cycles, and the overall distance traveled is averaged. Each experiment

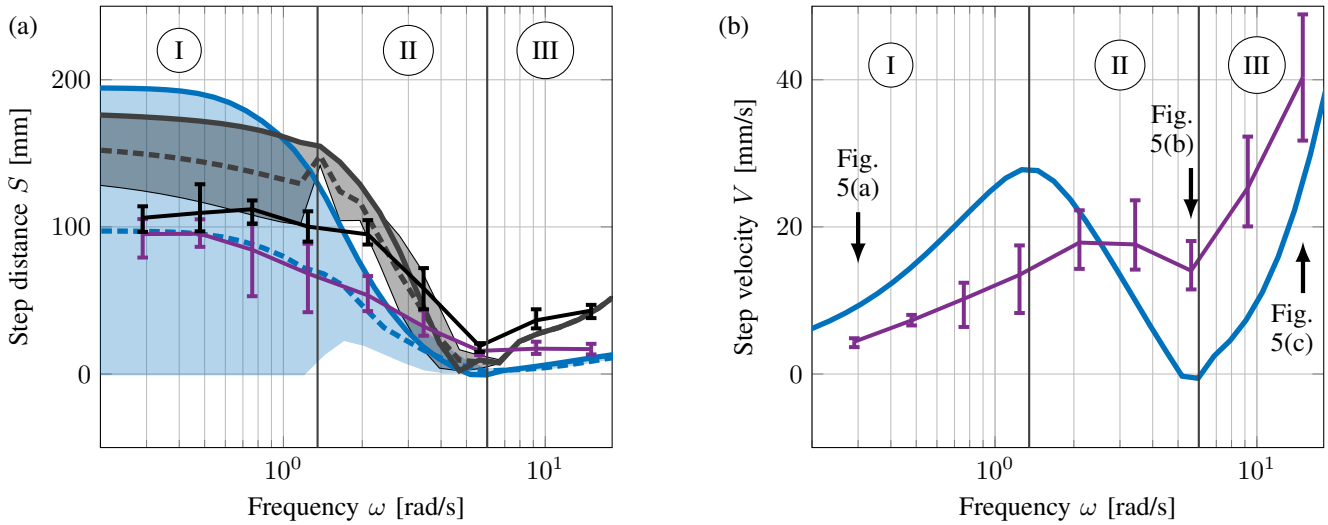


Fig. 4: Gait performance versus frequency – (a) Distance per step. (b) Average velocity. For constant $\psi = 20^\circ$: **nominal-friction simulation results (solid blue)**, $\mu_1/\mu_2 \in [0.9, 1.1]$ (blue area), **uncertain-friction distance S_μ (dashed blue)** and **experiment results with error-bars (purple)**. For $\psi = \psi_\mu^*(\omega)$ phase of optimal S_μ : **nominal-friction simulation results (gray)**, $\mu_1/\mu_2 \in [0.9, 1.1]$ (gray area), **uncertain-friction distance S_μ (dashed gray)** and **experiment results with error-bars (black)**

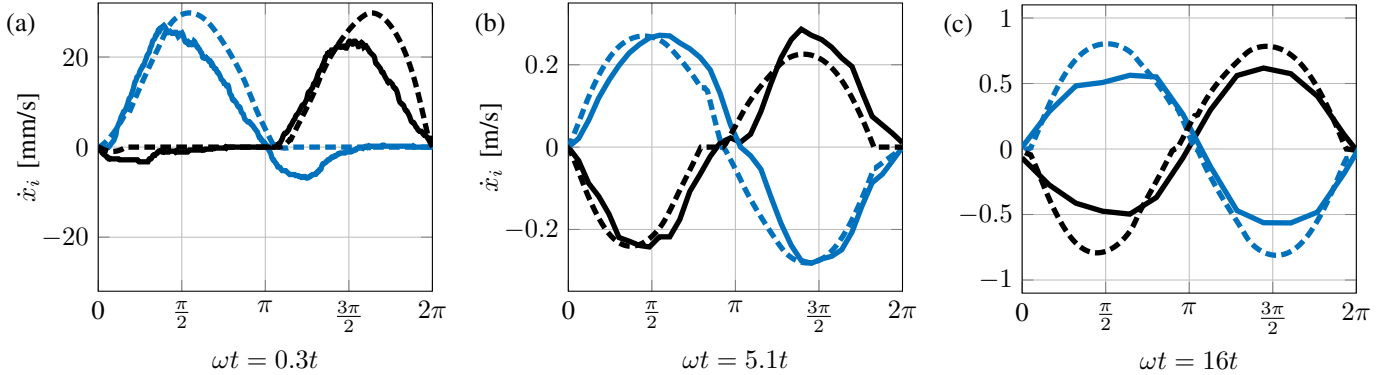


Fig. 5: Contacts' velocities \dot{x}_1 (blue) and \dot{x}_2 (black) – experiment results (solid curves) and simulation results (dashed curves). (a) $\omega = 0.3$ [rad/s] low frequency range (I). (b) $\omega = 5.1$ [rad/s] frequency range (II). (c) $\omega = 16$ [rad/s] high frequency range (III)

Parameter	Notation	Value	Units
Central link's mass	m_0	194	gr
Central link's length	l_0	187	mm
Central link's moment of inertia	J_0	776.3	kg mm ²
Distal links' mass	$m_1 = m_2 = m$	21	gr
Distal links' length	$l_1 = l_2 = l$	170	mm
Distal links' moment of inertia	$J_1 = J_2 = J$	98.7	kg mm ²
Friction coefficient – hard tips	μ	0.172	–
Friction coefficient – soft tips	μ	0.398	–

TABLE I: Summary of experimental setup parameters' values

is repeated four times, giving the black curve and error bars (representing the range of observations) in Fig.4. The qualitative performance in frequency is very similar to the analytical prediction, giving multiple local extrema in average velocity V in Fig.4(b). Yet, the actual distance traveled at the low frequencies range is about two times smaller than the simulation predicts. The differences can be explained by sensitivity analysis to friction variations, which we study in the next section VI. We will show that robustness to friction uncertainties has major influence and must be considered in order to improve the predictive power of the model and simulations.

By differentiating the measured horizontal position of the contacts, and filtering with moving average, we get the contacts' velocities $\dot{x}_i(t)$ for selected frequencies in solid curves in Fig. 5. It is observed that at low frequencies (Fig. 5(a)) slippage occurs in the undesired direction, resulting in a smaller net

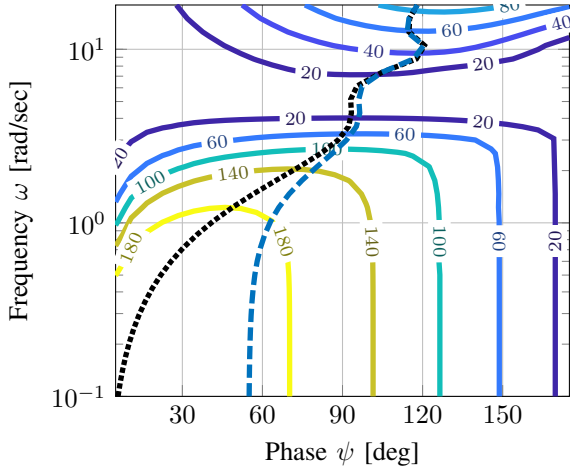


Fig. 6: Step distance S [mm] (contour plot) in parametric space ψ – ω . Phase $\psi^*(\omega)$ of optimal nominal-friction distance S (dotted black curve), phase $\psi_\mu^*(\omega)$ of optimal uncertain-friction distance S_μ (dashed blue curve)

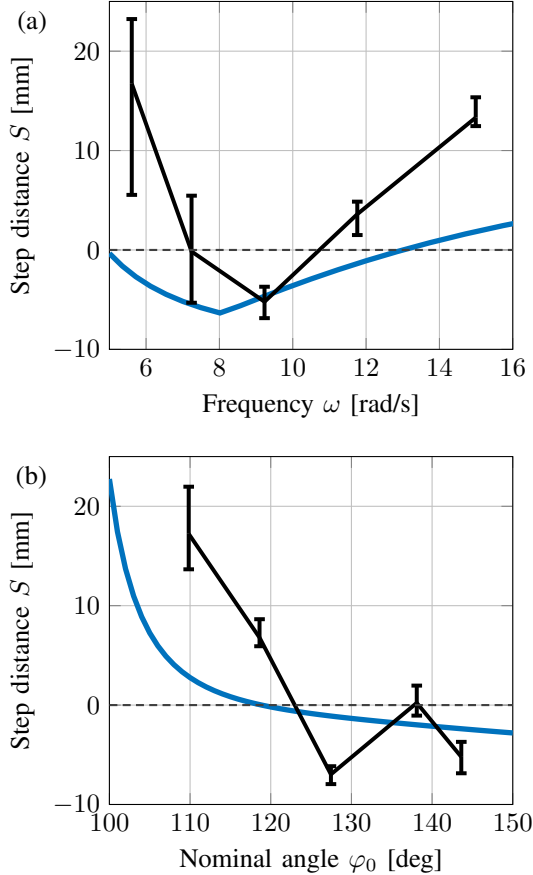


Fig. 7: Direction reversal – simulation results (blue) and experiment results with error-bars (black). (a) Step distance versus frequency for $\varphi_0 = 145^\circ$. (b) Step distance versus nominal angle for $\omega = 9$ [rad/s]

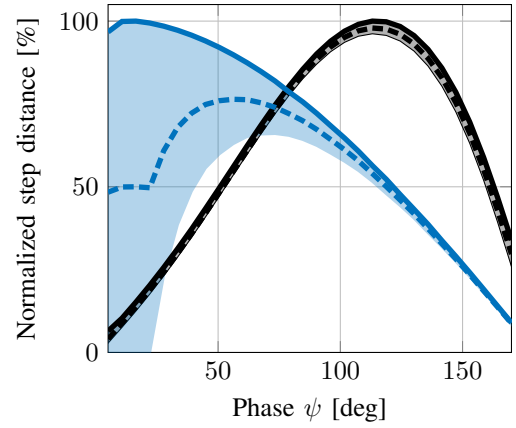


Fig. 8: Normalized step distance $S/\max\{S\}$ versus phase difference – nominal-friction distance S (solid curves), $\mu_1/\mu_2 \in [0.9, 1.1]$ (shaded areas) and uncertain-friction distance S_μ (dashed curves). $\omega = 0.3$ [rad/s] in blue and $\omega = 16$ [rad/s] in black

traveling distance than predicted. This small but significant divergence from the analytical model can also be explained by friction uncertainties (see Section VI). For higher frequencies (Fig. 5(b) and (c)), the experimental and analytical results match both qualitatively and quantitatively.

Finally, the phenomenon of direction reversal with variation of the nominal angle φ_0 is also achieved in experiments (black curves in Fig. 7) – see supplementary video [19]. It is of note that this experiment required switching the robot’s tips to softer material, with higher friction coefficient, which exhibits more robust behavior at this frequency range. The friction coefficient was measured (see Table I) and simulated in the corresponding blue curves in Fig. 7).

VI. ROBUSTNESS TO FRICTION UNCERTAINTIES

Based on the results from our experiments and previous works [14], [20], practical considerations suggest that the simulation predictions must be tested for sensitivity to inaccuracies in friction. Modeling (or measuring) and simulating the actual distribution of the friction along various surfaces involves increased complexity. In this section we propose a deterministic and computationally-cheap criterion, which captures the effects of uneven friction, and allows for numerical optimization. We perform the sensitivity analysis by varying the friction coefficients at each of the two contacts such that $\mu_i \in [1 - \varepsilon, 1 + \varepsilon]\mu$ (where μ_i is the coefficient at contact i and μ is the nominal measured coefficient). A symmetric perturbation $\mu_1 = \mu_2 = (1 \pm \varepsilon)\mu$ was found to insignificantly affect the distance S for reasonable ε (not shown). However, for an asymmetric perturbation, Fig. 4 shows in the shaded blue area how the distance S decreases as $\mu_1/\mu_2 \rightarrow 1 \pm \varepsilon$ for $\varepsilon = 0.1$ (which is close to the actual range measured in calibration experiments). Assuming the friction varies along the gait and among the strides within this uncertainty range (i.e. within the shaded area), we propose the following empirical computationally-simple criterion of robustness to uncertainties

in friction

$$S_\mu = \frac{1}{2} (S_{\min} + S_{\max}), \quad (6)$$

where

$$S_{\min/\max} = \min / \max \{S_{\mu_i \in [1-\varepsilon, 1+\varepsilon]\mu}\}. \quad (7)$$

This *uncertain-friction distance* is in fact the mean of the possible distances in the shaded area, as depicted by the dashed blue curve in Fig. 4(a). We observe that S_μ falls with excellent agreement to the experimental results, proving the validity of the proposed criterion. Furthermore, the width of the experiments' error bars, that represent the variance of the measurements, agree qualitatively with the width of the shaded area – hence, this analysis also predicts the repeatability of the gaits. Note that the following legend is consistent in all graphs analysing the step distance (i.e. Fig. 4(a), 8 and 9): the solid curve depicts the *nominal-friction distance* S (without friction perturbations), the shaded area (of similar color) shows the range of S for friction perturbation $\mu_1/\mu_2 \rightarrow 1 \pm \varepsilon$ and the dashed curve (of similar color) depicts S_μ . A solid curve connecting error bars (if exists) shows the experimental results in the corresponding parameters.

We deduce that the low frequency range is highly sensitive to friction uncertainties, while increasing the actuation frequency allows for gaits with similar (and even higher) average velocity that show smaller sensitivity, thus having increased robustness to variations in surface friction. Further analyzing the robustness via the proposed criterion S_μ , shows that significant improvement can be achieved at low frequencies by optimizing the phase difference. This is illustrated in Fig. 8 for $\omega = 0.3$ [rad/s] (in blue) and $\omega = 16$ [rad/s] (in black), normalized by the maximal S (since the dimensional S for $\omega = 16$ [rad/s] is much smaller). We see how at low frequencies choosing the phase $\psi = 16^\circ$ at the optimum of S (solid curve), results in a decrease of 50% in the presence of friction uncertainties, as indicated by S_μ (dashed curve). On the other hand, the optimum of S_μ at $\psi = 56^\circ$ gives only 24% decrease of the step distance, with much narrower shaded area – which shall result in less variance and more robust gait. As the frequency rises (black curves), S and S_μ become closer, as previously deduced. This is also illustrated by plotting $\psi_\mu^*(\omega)$, the optimal phase to maximize the uncertain-friction distance S_μ , in dashed blue curve over the $\psi - \omega$ map in Fig. 6. Note how this curve merges with $\psi^*(\omega)$, the optimal phase to maximize the nominal-friction distance S (dotted black curve), at high frequencies, which we have seen to be naturally robust from the dynamics of the system.

In Fig. 9 we study the gaits' performance under uncertainties in friction for various frequencies, at phase $\psi^*(\omega)$ (in blue) versus at phase $\psi_\mu^*(\omega)$ (in black). Though the nominal-friction distance S (solid curves), which is the optimistic prediction for perfectly even friction, is slightly lower for $\psi = \psi_\mu^*$, the uncertain-friction distance S_μ (dashed curves), which was shown to be a realistic prediction, is significantly improved at low frequencies. The experimental results for $\psi = \psi_\mu^*$ are plotted in Fig. 4(a) by a black curve with error bars. We see significant improvement of the distance and repeatability,

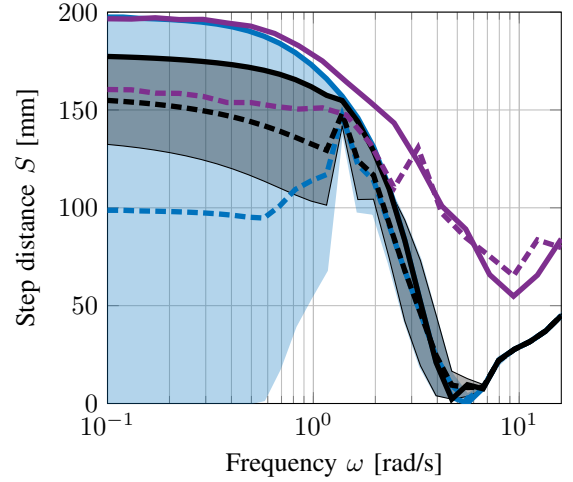


Fig. 9: Step distance versus frequency – nominal-friction distance S (solid curves), $\mu_1/\mu_2 \in [0.9, 1.1]$ (shaded areas) and uncertain-friction distance S_μ (dashed curves). Optimization ($\psi^*(\omega)$) of the nominal-friction distance S in blue and optimization ($\psi_\mu^*(\omega)$) of the uncertain-friction distance S_μ in black. Optimization of the nominal-friction distance S (solid purple curve) and S_μ (dashed purple curve) with inputs' time scaling

compared to unoptimized gaits for $\psi = 20^\circ$ in purple curve. Comparing these observations to the analytical prediction in gray curves (which are the same as the black curves in Fig. 9) we see excellent agreement at high frequencies. At low frequencies the improvement is smaller than predicted by the model and our uncertain-friction criterion.

VII. MASS ASYMMETRY AND TIME-SCALING INPUT SHAPING

In this section we investigate the influence of mass distribution on the step distance S and discover the effects of asymmetry. We introduce a time-scaling input shaping strategy, which achieves asymmetry without mechanical changes to the robot, and utilize machine-learning algorithm to optimize the parameters of such inputs.

Considering the ratio between the mass of the distal and center links $\frac{1}{2}(m_1 + m_2)/m_0$, the distance S grows almost monotonically with the decrease of the distal links' mass (see Appendix). A more divergent and influential parameter is the asymmetry of mass distribution among the distal links m_1/m_2 (also shown in Supplemental material). Hereafter we also keep fixed amplitude $A = 18^\circ$ and nominal angle $\varphi_0 = 110^\circ$, in order to investigate only the effect of asymmetry. At the low frequencies range ($\omega \lesssim 1$ [rad/s]), the gaits are highly sensitive to asymmetry in any direction, causing significant decrease in S . As the frequency increases, the sensitivity is reduced and asymmetric mass distribution even becomes advantageous. The preference moves from heavier front link $m_1 > m_2$ at mid-range frequencies (where even direction reversal occurs) to heavier rear link $m_2 > m_1$ at high frequencies. Exploiting the advantages of asymmetric mass distribution requires mechanically reassembling the robot for each frequency. Therefore, we

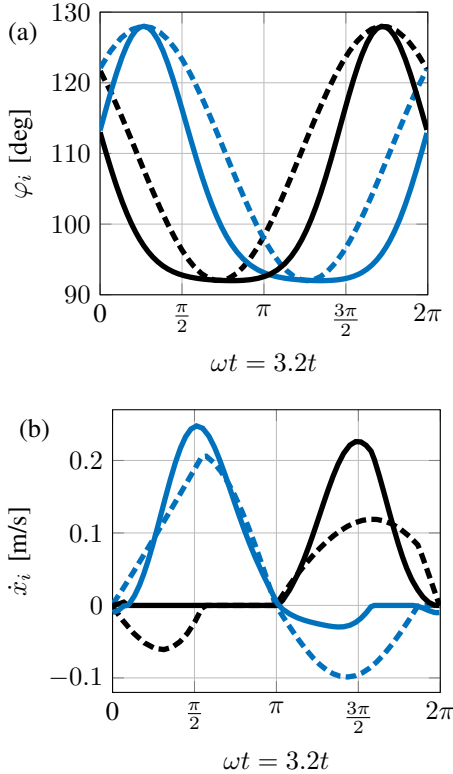


Fig. 10: Gait with time-scaling (solid curves) and without time-scaling $\alpha = 0$ (dashed curves) for $\omega = 3.2$ [rad/s]. (a) Joint angles φ_1 (blue) and φ_2 (black). (b) Contacts' velocities \dot{x}_1 (blue) and \dot{x}_2 (black)

desire to achieve a similar improvement effect of the distance S by shaping the input signals $\varphi_i(t)$.

We propose a *time-scaling* strategy, where the joint angles remain of the form $\varphi_i(t) = \varphi_0 + A \sin(s(\omega t \pm \psi/2))$ as in (5), but a time-scaling function $s(\xi)$ is introduced as

$$s(\xi) = \xi + \alpha \sin(\xi + \Upsilon). \quad (8)$$

For $\alpha = 0$ these functions are reduced to the unscaled case of (5), but $\alpha \neq 0$ generates an uneven ‘‘internal’’ pace in $\varphi_i(s(t))$, while preserving the overall shape and the principal harmonic (as long as $\dot{s}(t) \geq 0$). This is illustrated in Fig. 10(a) for optimal $\psi = \psi^*$ without time-scaling $\alpha = 0$ (dashed curves), compared to optimal choice of both (α, Υ) to maximize S and same ψ^* (solid curves), at $\omega = 3.2$ [rad/s]. Fig. 10(b) shows how these time-scaled inputs significantly improve S by both increasing $\dot{x}_i(t)$ in the advancement direction and reducing slippage in the opposing direction. At this frequency, the optimal scaled input achieves this improvement by extending the legs rapidly and retracting them slowly (see supplementary video [19]).

Since the system is highly nonlinear and non-smooth, induced by the hybrid contact-state transitions, finding optimal values of multiple parameters involves increased complexity. Gradient-based optimization algorithms (like Newton’s method or gradient descent) struggle and typically converge to a local minimum, which depends on the basin of attraction

the starting point [22]. To search for global optimum, optimizations must be initialized from multiple points, which is time-consuming (we attempted to use MATLAB® `fmincon` with `multistart`). Contrarily, *Bayesian optimization* is a *machine-learning* approach which is based on fitting a Gaussian process [23]. This algorithm was shown to be very efficient for legged robotic locomotion [22], [24], probably since such systems exhibit non-smooth behavior and coupling of parameters. We applied this machine-learning algorithm (via MATLAB® `bayesopt`) to our numerical simulation, described in Section IV, and achieved rapid and stable convergence (compared to gradient-based methods). Fig. 9 illustrates the machine-learning optimization of time-scaling parameters and phase difference (α, Υ, ψ) to maximize S (solid purple curve) and S_μ (dashed purple curve) for various frequencies. A significant improvement of S is achieved at the middle- and high-frequency ranges.

VIII. HYBRID FEEDBACK CONTROL

In the approach presented so far, we prescribed harmonic input signals to the actuated joints and optimize their parameters, assuming minimal sensing and computation abilities (just the closed-loop control of the servos). This often leads to undesired slippage, which reduces the distance the robot travels. An alternative approach is to prescribe a feedback control law, which utilizes sensing of the contacts’ velocities to eliminate undesired slippage. Most existing works on slippage in robotic locomotion, either slippage detection and recovery [25] or avoidance (for quasistatic locomotion) [26], deal with systems with higher dimensionality, which allows to stabilize the robots’ main body separately from the contacts. The inchworm crawling locomotion has inherent continuous slippage, and the three-link robot has very few DoF and hence requires a different method.

We propose a hybrid (contacts state-based) feedback control law, based on PD reference tracking with inverse dynamics [21], assuming the whole state $\mathbf{q}, \dot{\mathbf{q}}$ can be measured (including contacts’ velocities \dot{x}_i). Once slip-slip state is detected (indicating undesired slippage), the hybrid control switches from tracking of a reference trajectory $\mathbf{q}_c(t)$ in (5) to tracking of ‘‘ideal’’ contacts velocities. The detailed derivation is given in the Appendix. Remarkably, simulation results of this control law show drastic improvement of travelled distance by suppressing undesired slippage (see Appendix for examples). Nevertheless, the results require careful tuneup and currently work only for a range of reference input frequencies. We deduce that for high frequencies the three-link robot’s slippage is strongly enforced by the natural dynamics of the contact and can hardly be eliminated. For most parameter values the control struggles to overcome slippage, which results in either loss of contact or worse performance than without feedback. These limitation can perhaps be solved by forces sensing-based control [27] and additional actuation.

IX. CONCLUDING DISCUSSION

This paper has addressed modeling of dynamic robotic inchworm-like crawling with passive frictional contacts. Such

locomotion is sensitive to uncertainties in the friction, but once that is accounted for (with a minimal analysis we propose) the model shows good agreement with experimental results.

The model also allows for comprehension of the influence of inertia and other phenomena. For example it is observed that with low-frequency actuation, tuning the gait's parameters according to the criterion we proposed can significantly improve the robustness with respect to variations and unevenness in surface friction. At high frequencies the gaits demonstrate natural robustness with even higher average velocities.

The quasistatic low-frequency range was also observed to be very sensitive to asymmetry. However, as the frequency rises asymmetry can actually be exploited to improve the gaits' performance in traveling distance. Similar effect was also created by shaping the inputs with time-scaling technique, without mechanical changes to the robot. A feedback control, based on the contacts state, was also proposed. Though this approach can reduce undesired slippage for some cases, in general it struggles for the three-link configuration, and requires more advanced sensing and computation. Future research may address this with additional DoF and actuation or sensing of the contact forces.

The latter analyses were only investigated in simulation. Experimentally testing the optimizations proposed in Sections VI and VII and the control in Section VIII on this and other legged robots shall also be the subject of future research.

The presented notions can be implemented in future into soft crawling robots, both quasistatic and dynamic. We also believe that crawling locomotion in articulated legged robots is advantageous and can be exploited more extensively. Finally, just as McGeer's biped [15] was an inspiration to studies of simple and energetically efficient control, we hope that our three-link model will pave the way for future analytic and experimental works in inertial crawling locomotion.

REFERENCES

- [1] P.-B. Wieber, R. Tedrake, S. Kuindersma, Modeling and control of legged robots, in: Springer handbook of robotics, Springer, 2016, pp. 1203–1234.
- [2] S. Kim, C. Laschi, B. Trimmer, Soft robotics: a bioinspired evolution in robotics, *Trends in Biotechnology* 31 (5) (2013) 287–294.
- [3] K. Kotay, D. Rus, The inchworm robot: A multi-functional system, *Autonomous Robots* 8 (1) (2000) 53–69.
- [4] Q. Wu, T. G. D. Jimenez, J. Qu, C. Zhao, X. Liu, Regulating surface traction of a soft robot through electrostatic adhesion control, in: *Int. Conf. on Intelligent Robots and Systems (IROS), IEEE/RSJ, 2017*, pp. 488–493.
- [5] J.-S. Koh, K.-J. Cho, Omegabot: Biomimetic inchworm robot using SMA coil actuator and smart composite microstructures (SCM), in: *Int. Conf. on Robotics and Biomimetics (ROBIO), IEEE, 2009*, pp. 1154–1159.
- [6] S. M. Felton, M. T. Tolley, C. D. Onal, D. Rus, R. J. Wood, Robot self-assembly by folding: A printed inchworm robot, in: *Int. Conf. on Robotics and Automation (ICRA), IEEE, 2013*, pp. 277–282.
- [7] J. Wang, J. Min, Y. Fei, W. Pang, Study on nonlinear crawling locomotion of modular differential drive soft robot, *Nonlinear Dynamics* (2019) 1–17.
- [8] V. Vikas, E. Cohen, R. Grassi, C. Sozer, B. Trimmer, Design and locomotion control of a soft robot using friction manipulation and motor-tendon actuation., *IEEE Transaction on Robotics* 32 (4) (2016) 949–959.
- [9] T. Umedachi, V. Vikas, B. A. Trimmer, Highly deformable 3-D printed soft robot generating inching and crawling locomotions with variable friction legs, in: *Int. Conf. on Intelligent Robots and Systems (IROS), IEEE/RSJ, 2013*, pp. 4590–4595.
- [10] H. Guo, J. Zhang, T. Wang, Y. Li, J. Hong, Y. Li, Design and control of an inchworm-inspired soft robot with Omega-arching locomotion, in: *Int. Conf. on Robotics and Automation (ICRA), IEEE, 2017*, pp. 4154–4159.
- [11] S. Chen, Y. Cao, M. Sarparast, H. Yuan, L. Dong, X. Tan, C. Cao, Soft crawling robots: Design, actuation, and locomotion, *Advanced Materials Technologies* 5 (2) (2020) 1900837.
- [12] D. Trivedi, C. D. Rahn, W. M. Kier, I. D. Walker, Soft robotics: Biological inspiration, state of the art, and future research, *Applied Bionics and Biomechanics* 5 (3) (2008) 99–117.
- [13] S. Miyashita, S. Guitron, M. Ludersdorfer, C. R. Sung, D. Rus, An untethered miniature origami robot that self-folds, walks, swims, and degrades, in: *Int. Conf. on Robotics and Automation (ICRA), IEEE, 2015*, pp. 1490–1496.
- [14] B. Gamus, L. Salem, A. Gat, Y. Or, Understanding inchworm crawling for soft-robotics, *IEEE Robotics and Automation Letters* 5 (2) (2020) 1397–1404. doi:10.1109/LRA.2020.2966407.
- [15] T. McGeer, et al., Passive dynamic walking, *The Int. J. of Robotics Research* 9 (2) (1990) 62–82.
- [16] J. Yao, S. Gao, G. Jiang, T. L. Hill, H. Yu, D. Shao, Screw theory based motion analysis for an inchworm-like climbing robot, *Robotica* 33 (8) (2015) 1704–1717.
- [17] A. Ghanbari, S. Noorani, Optimal trajectory planning for design of a crawling gait in a robot using genetic algorithm, *Int. J. of Advanced Robotic Systems* 8 (1) (2011) 6.
- [18] R. Goebel, R. G. Sanfelice, A. R. Teel, Hybrid dynamical systems, *Control Systems Magazine* 29 (2) (2009) 28–93.
- [19] Supplemental video at <https://youtu.be/8Y4mvwLYnKY>.
- [20] C. Majidi, R. F. Shepherd, R. K. Kramer, G. M. Whitesides, R. J. Wood, Influence of surface traction on soft robot undulation, *The Int. J. of Robotics Research* 32 (13) (2013) 1577–1584.
- [21] R. M. Murray, Z. Li, S. S. Sastry, S. S. Sastry, A mathematical introduction to robotic manipulation, CRC press, 1994.
- [22] R. Calandra, A. Seyfarth, J. Peters, M. P. Deisenroth, An experimental comparison of bayesian optimization for bipedal locomotion, in: *Int. Conf. on Robotics and Automation (ICRA), IEEE, 2014*, pp. 1951–1958.
- [23] C. E. Rasmussen, Gaussian processes in machine learning, in: *Summer School on Machine Learning, Springer, 2003*, pp. 63–71.
- [24] M. Tesch, J. Schneider, H. Choset, Using response surfaces and expected improvement to optimize snake robot gait parameters, in: *Int. Conf. on Intelligent Robots and Systems (IROS), IEEE/RSJ, 2011*, pp. 1069–1074.
- [25] H. Takemura, M. Deguchi, J. Ueda, Y. Matsumoto, T. Ogasawara, Slip-adaptive walk of quadruped robot, *Robotics and Autonomous Systems* 53 (2) (2005) 124–141.
- [26] S. Samadi, S. Caron, A. Tanguy, A. Kheddar, Balance of humanoid robot in multi-contact and sliding scenarios, in: *Int. Conf. on Robotics and Automation (ICRA), 2020*.
- [27] K. Kojima, S. Nozawa, K. Okada, M. Inaba, Shuffle motion for humanoid robot by sole load distribution and foot force control, in: *Int. Conf. on Intelligent Robots and Systems (IROS), IEEE, 2015*, pp. 2187–2194.

$$\mathbf{M} = \begin{bmatrix} m_0 + 2m & 0 & \frac{lm}{2}(s_1 + s_2) & -\frac{lm}{2}s_1 & \frac{lm}{2}s_2 \\ 0 & m_0 + 2m & \frac{lm}{2}(c_1 - c_2) & -\frac{lm}{2}c_1 & -\frac{lm}{2}c_2 \\ \frac{lm}{2}(s_1 + s_2) & \frac{lm}{2}(c_1 - c_2) & \mathbf{M}_{3,3} & \frac{lm}{4}(l_0 \cos \varphi_1 - l) - J & J + \frac{lm}{4}(l - l_0 \cos \varphi_2) \\ -\frac{lm}{2}s_1 & -\frac{lm}{2}c_1 & \frac{lm}{4}(l_0 \cos \varphi_1 - l) - J & \frac{l^2 m}{4} + J & 0 \\ \frac{lm}{2}s_2 & -\frac{lm}{2}c_2 & J + \frac{lm}{4}(l - l_0 \cos \varphi_2) & 0 & \frac{l^2 m}{4} + J \end{bmatrix} \quad (9)$$

APPENDIX

Motion equations

The terms for the matrices in the dynamic motion equations (3) are as follows: the mass matrix \mathbf{M} is given in (9), where $\mathbf{M}_{3,3} = 2J + J_0 + \frac{m}{2}(l_0^2 + l^2 - l_0 l \cos \varphi_1 - l_0 l \cos \varphi_2)$ and the abbreviations $s_1 \equiv \sin(\varphi_1 - \theta)$, $s_2 \equiv \sin(\varphi_2 + \theta)$, $c_1 \equiv \cos(\varphi_1 - \theta)$ and $c_2 \equiv \cos(\varphi_2 + \theta)$. Also

$$\mathbf{B} = \frac{1}{2}lm \begin{bmatrix} (\dot{\varphi}_2 + \dot{\theta})^2 c_2 - (\dot{\varphi}_1 - \dot{\theta})^2 c_1 \\ (\dot{\varphi}_2 + \dot{\theta})^2 s_2 - (\dot{\varphi}_1 + \dot{\theta})^2 s_1 \\ \mathbf{B}_3 \\ -\frac{1}{2}l_0 \dot{\theta}^2 \sin \varphi_1 \\ -\frac{1}{2}l_0 \dot{\theta}^2 \sin \varphi_2 \end{bmatrix}, \quad (10)$$

where $\mathbf{B}_3 = \frac{1}{2}l_0((2\dot{\theta}\dot{\varphi}_1 - \dot{\varphi}_1^2) \sin \varphi_1 + (\dot{\varphi}_2^2 + 2\dot{\theta}\dot{\varphi}_2) \sin \varphi_2)$, and

$$\mathbf{G} = g \begin{bmatrix} 0 \\ m_0 + 2m \\ \frac{1}{2}lm(c_1 - c_2) \\ -\frac{1}{2}lmc_1 \\ -\frac{1}{2}lmc_2 \end{bmatrix}. \quad (11)$$

The Jacobians in (2) are

$$\mathbf{W}_1 \equiv \begin{bmatrix} \mathbf{w}_1^x \\ \mathbf{w}_1^y \end{bmatrix} = \begin{bmatrix} 1 & 0 & \frac{1}{2}(2ls_1 + l_0 \sin \theta) & -ls_1 & 0 \\ 0 & 1 & \frac{1}{2}(2lc_1 - l_0 \cos \theta) & -lc_1 & 0 \end{bmatrix} \quad (12)$$

and

$$\mathbf{W}_2 \equiv \begin{bmatrix} \mathbf{w}_2^x \\ \mathbf{w}_2^y \end{bmatrix} = \begin{bmatrix} 1 & 0 & \frac{1}{2}(2ls_2 - l_0 \sin \theta) & 0 & ls_2 \\ 0 & 1 & -\frac{1}{2}(2lc_2 - l_0 \cos \theta) & 0 & -lc_2 \end{bmatrix}. \quad (13)$$

When one of the contacts is at slippage while the other maintains contact sticking – for concreteness let us consider stick-slip contact-state – from (1) we get three kinematic constraints: contact-sticking of one leg $\mathbf{v}_1 = \mathbf{W}_1 \dot{\mathbf{q}} = 0$ and no-detachment of the slipping leg $\dot{y}_2 = \mathbf{w}_2^y \dot{\mathbf{q}} = 0$. Differentiating these constraints with respect to time gives

$$\begin{bmatrix} \mathbf{W}_1 \\ \mathbf{w}_2^y \end{bmatrix} \ddot{\mathbf{q}} = - \begin{bmatrix} \dot{\mathbf{W}}_1 \\ \dot{\mathbf{w}}_2^y \end{bmatrix} \dot{\mathbf{q}}. \quad (14)$$

We can now formulate the dynamic equations (3) with the constraints (14) as

$$\begin{bmatrix} \mathbf{M} & -\mathbf{W}_1^T & -\mathbf{W}_2^T \Gamma_2 \\ \mathbf{W}_1 & 0 & 0 \\ \mathbf{w}_2^y & 0 & 0 \end{bmatrix} \begin{bmatrix} \ddot{\mathbf{q}} \\ f_1^x \\ f_1^y \\ f_2^y \end{bmatrix} = \begin{bmatrix} -\mathbf{B} - \mathbf{G} + \mathbf{E}\tau \\ -\dot{\mathbf{W}}_1 \dot{\mathbf{q}} \\ -\dot{\mathbf{w}}_2^y \dot{\mathbf{q}} \end{bmatrix}, \quad (15)$$

where

$$\Gamma_i \equiv \begin{bmatrix} -\mu \text{sign } \dot{x}_i \\ 0 \end{bmatrix}, \quad (16)$$

for the contact at slippage from (4b).

Slip-slip contact state is formulated similarly to (15), though the contact forces of both contacts maintain (16) and the constraints are reduced to no-detachment only $\dot{y}_1 = \dot{y}_2 = 0$, giving

$$\begin{bmatrix} \mathbf{M} & -\mathbf{W}_1^T \Gamma_1 & -\mathbf{W}_2^T \Gamma_2 \\ \mathbf{w}_1^y & 0 & 0 \\ \mathbf{w}_2^y & 0 & 0 \end{bmatrix} \begin{bmatrix} \ddot{\mathbf{q}} \\ f_1^y \\ f_2^y \end{bmatrix} = \begin{bmatrix} -\mathbf{B} - \mathbf{G} + \mathbf{E}\tau \\ -\dot{\mathbf{w}}_1^y \dot{\mathbf{q}} \\ -\dot{\mathbf{w}}_2^y \dot{\mathbf{q}} \end{bmatrix}. \quad (17)$$

The mass and Jacobian matrices can be decomposed into blocks corresponding to the constrained- and body-coordinates as $\mathbf{M} = [\mathbf{M}_c \ \mathbf{M}_b]$ and $\mathbf{W}_i = [\{\mathbf{W}_i\}_c \ \{\mathbf{W}_i\}_b]$. Then we can rearrange (15) and (17) such that all the unknowns are on one side as (only the formulation of stick-slip in (15) shown for brevity)

$$\begin{bmatrix} \mathbf{M}_b & -\mathbf{E} & -\mathbf{W}_1^T & -\mathbf{W}_2^T \Gamma_2 \\ \{\mathbf{W}_1\}_b & 0 & 0 & 0 \\ \{\mathbf{W}_2\}_b & 0 & 0 & 0 \end{bmatrix} \begin{bmatrix} \ddot{\mathbf{q}}_b \\ \tau \\ f_1^x \\ f_1^y \\ f_2^y \end{bmatrix} = \begin{bmatrix} -\mathbf{M}_c \\ -\{\mathbf{W}_1\}_c \\ -\{\mathbf{w}_2^y\}_c \end{bmatrix} \ddot{\mathbf{q}}_c + \begin{bmatrix} -\mathbf{B} - \mathbf{G} \\ -\dot{\mathbf{W}}_1 \dot{\mathbf{q}} \\ -\dot{\mathbf{w}}_2^y \dot{\mathbf{q}} \end{bmatrix}. \quad (18)$$

Finally, for a state-vector $\mathbf{x}(t) = [\mathbf{q}_b^T \ \dot{\mathbf{q}}_b^T]^T$ and prescribed $\mathbf{q}_c(t)$, $\dot{\mathbf{q}}_c(t)$, $\ddot{\mathbf{q}}_c(t)$, we get a series of complete first order ODEs.

Mass distribution colormaps

In Fig. 11 we present complete colormaps of the step distance S the versus mass distribution in both parameters – ratio of distal to center links' mass and asymmetry among the distal links. We also keep fixed amplitude $A = 18^\circ$ and nominal angle $\varphi_0 = 110^\circ$, in order to investigate only

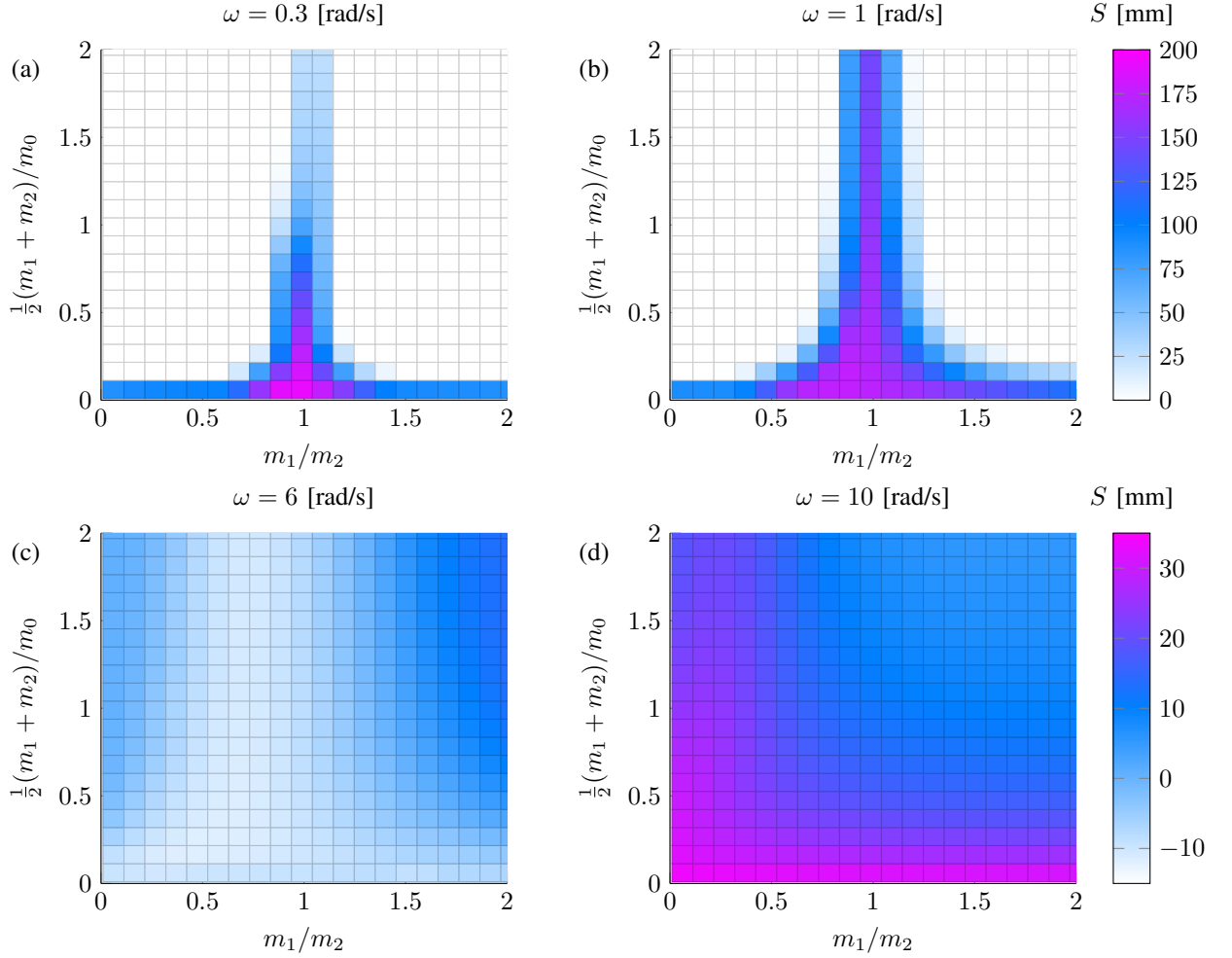


Fig. 11: Colormaps of step distance S versus mass distribution for various frequencies – Distal-to-center links' mass ratio $\frac{1}{2}(m_1 + m_2)/m_0$ versus asymmetry ratio m_1/m_2

the mass distribution. Fig. 12 depicts the effect of asymmetry in mass distribution among the distal links m_1/m_2 , for various frequencies and constant ratio to the central link $\frac{1}{2}(m_1 + m_2)/m_0 = 0.5$. Note that these curves are actually a section of the colormaps for selected frequencies.

Feedback control with hybrid inverse dynamics

Assuming we can measure the whole state $\mathbf{q}, \dot{\mathbf{q}}$, including contacts' velocities \dot{x}_i , which allows to deduce the contacts states, we propose the following control strategy: First, we now prescribe $\ddot{\mathbf{q}}_c(t, \mathbf{q}, \dot{\mathbf{q}})$ as the controlled input (instead of prescribing $\mathbf{q}_c(t)$ and its derivatives as before). We calculate an “ideal” reference trajectory of the contacts velocities $\mathbf{v}_x^r(t) = [\dot{x}_1^r(t) \ \dot{x}_2^r(t)]^T$ in which each contact slips for half of the cycle in the advancement direction only, and which corresponds to the reference joints trajectories $\mathbf{q}_c^r(t)$ in (5). As long as the contacts states are stick-slip or slip-stick, the contacts velocities $\mathbf{v}_x^r(t)$ are maintained kinematically from the joint trajectories $\mathbf{q}_c^r(t)$. In these states we utilize PD reference tracking control law [21]. When slip-slip state is detected, it

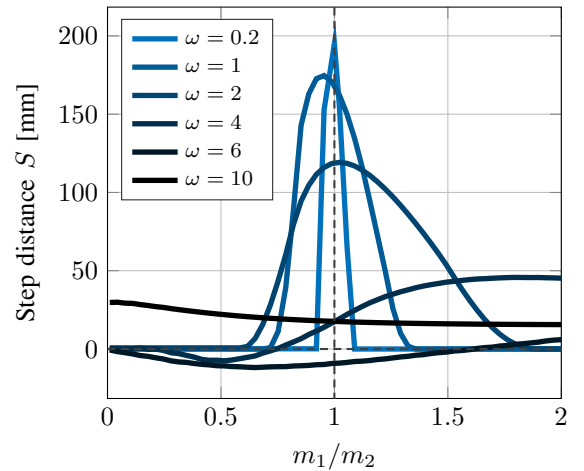


Fig. 12: Step distance versus mass asymmetry m_1/m_2 for various frequencies ω and constant $\frac{1}{2}(m_1 + m_2)/m_0 = 0.5$

indicates undesired slippage. The control law is then *switched* to PD reference tracking of $\mathbf{v}_r^x(t)$, translated with inverse dynamics [21] to the joints' inputs $\ddot{\mathbf{q}}_c(t)$ (detailed derivation follows). When trying to enforce $\mathbf{v}_r^x(t)$, this control law often results in limit configuration, causing ground-collision or tipping over. Hence another switch is introduced – if either angle exceeds a predefined limit $\varphi_i \in [\varphi_{min}, \varphi_{max}] \equiv \Phi$, the control law changes back to reference tracking of $\mathbf{q}_c(t)^r$. Overall the control law is

$$\ddot{\mathbf{q}}_c = \begin{cases} \mathbf{S}_1^{-1} [\dot{\mathbf{v}}_r^x - \mathbf{K}_v(\mathbf{v}_x - \mathbf{v}_r^x) - \mathbf{S}_0] & \text{if slip-slip} \\ & \& \varphi_i \in \Phi \\ \ddot{\mathbf{q}}_c^r - \mathbf{K}_D(\dot{\mathbf{q}}_c - \dot{\mathbf{q}}_c^r) - \mathbf{K}_P(\mathbf{q}_c - \mathbf{q}_c^r) & \text{otherwise} \end{cases} \quad (19)$$

where \mathbf{K}_v , \mathbf{K}_P , \mathbf{K}_D are 2×2 positive-definite matrices of control gains $\mathbf{S}_0(\mathbf{q}, \dot{\mathbf{q}})$, $\mathbf{S}_1(\mathbf{q})$ are inverse dynamics matrices derived next.

We consider a constrained state equation like (18), for slip-slip contacts state

$$\begin{bmatrix} \mathbf{M}_b & -\mathbf{E} & -\mathbf{W}_1^T \Gamma_1 & -\mathbf{W}_2^T \Gamma_2 \\ \{\mathbf{w}_1^y\}_b & 0 & 0 & 0 \\ \{\mathbf{w}_2^y\}_b & 0 & 0 & 0 \end{bmatrix} \begin{bmatrix} \ddot{\mathbf{q}}_b \\ \tau \\ f_1^y \\ f_2^y \end{bmatrix} = \begin{bmatrix} -\mathbf{M}_c \\ -\{\mathbf{w}_1^y\}_c \\ -\{\mathbf{w}_2^y\}_c \end{bmatrix} \ddot{\mathbf{q}}_c + \begin{bmatrix} -\mathbf{B} - \mathbf{G} \\ -\dot{\mathbf{w}}_1^y \dot{\mathbf{q}} \\ -\dot{\mathbf{w}}_2^y \dot{\mathbf{q}} \end{bmatrix}, \quad (20)$$

which can be denoted as $\mathbf{A}(\mathbf{q})\mathbf{z} = \mathbf{b}(\mathbf{q}, \dot{\mathbf{q}}) + \mathbf{c}(\mathbf{q})\ddot{\mathbf{q}}_c$, where $\ddot{\mathbf{q}}_b = [\mathbf{I}_{3 \times 3} \ 0_{3 \times 5}]\mathbf{z} \equiv \mathbf{T}\mathbf{z}$. From (20) the body coordinates' accelerations $\ddot{\mathbf{q}}_b$ can be found for prescribed $\ddot{\mathbf{q}}_c$ and known state as

$$\ddot{\mathbf{q}}_b = \mathbf{T} \mathbf{A}^{-1}(\mathbf{q}) [\mathbf{b}(\mathbf{q}, \dot{\mathbf{q}}) + \mathbf{c}(\mathbf{q})\ddot{\mathbf{q}}_c]. \quad (21)$$

Next, the contacts velocities are written in terms of the the Jacobian

$$\mathbf{v}_x = \begin{bmatrix} \dot{x}_1 \\ \dot{x}_2 \end{bmatrix} = \begin{bmatrix} \mathbf{w}_1^x \\ \mathbf{w}_2^x \end{bmatrix} \dot{\mathbf{q}} \equiv \mathbf{W}^x \dot{\mathbf{q}}. \quad (22)$$

This can be differentiated and decomposed into constrained- and body-coordinates as

$$\dot{\mathbf{v}}_x = \begin{bmatrix} \ddot{x}_1 \\ \ddot{x}_2 \end{bmatrix} = \dot{\mathbf{W}}^x \dot{\mathbf{q}} + \mathbf{W}^x \ddot{\mathbf{q}} = \dot{\mathbf{W}}^x \dot{\mathbf{q}} + \mathbf{W}_b^x \ddot{\mathbf{q}}_b + \mathbf{W}_c^x \ddot{\mathbf{q}}_c. \quad (23)$$

Putting (21) into (23) gives a relation between the joints' and the contacts' accelerations of the form $\dot{\mathbf{v}}_x = \mathbf{S}_1(\mathbf{q})\ddot{\mathbf{q}}_c + \mathbf{S}_0(\mathbf{q}, \dot{\mathbf{q}})$, which defines the inverse dynamics matrices in the control law (19).

Proof of convergence: The joints' reference tracking law can immediately be rearranged as $\ddot{\mathbf{e}}_q + \mathbf{K}_D \dot{\mathbf{e}}_q + \mathbf{K}_P \mathbf{e}_q = 0$, where $\mathbf{e}_q(t) \equiv \mathbf{q}_c - \mathbf{q}_c^r$ is the joints' angles error, which we easily see to be converging (for positive-definite \mathbf{K}_P , \mathbf{K}_D). Putting the control law for contacts' velocities tracking (19) into (23) with (21), also gives a converging velocities error $\mathbf{e}_v(t) \equiv \mathbf{v}_x - \mathbf{v}_r^x$ of the form $\dot{\mathbf{e}}_v + \mathbf{K}_v \mathbf{e}_v = 0$. Of course this proof does not consider the the hybrid switching of the control law and the contact states, hence the convergence will only be local.

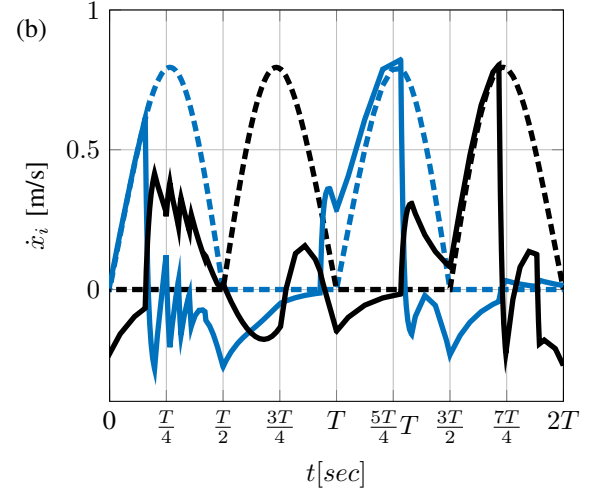
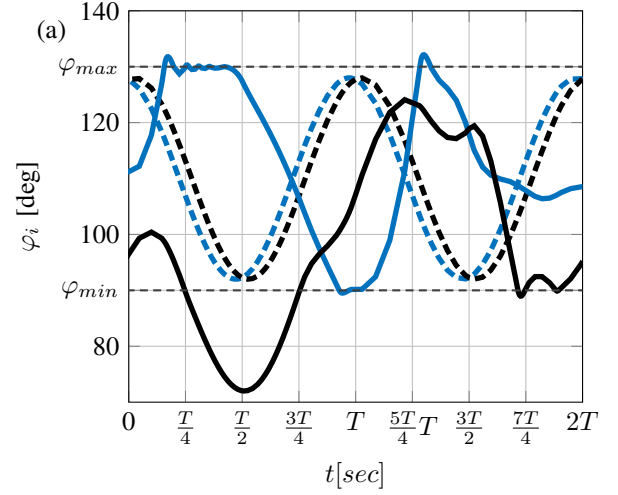


Fig. 13: Feedback control gait performance (solid curves) and reference trajectories (dashed curves) for $\omega = 8$ [rad/s]. (a) Joint angles φ_1 (blue) and φ_2 (black). (b) Contacts' velocities \dot{x}_1 (blue) and \dot{x}_2 (black)

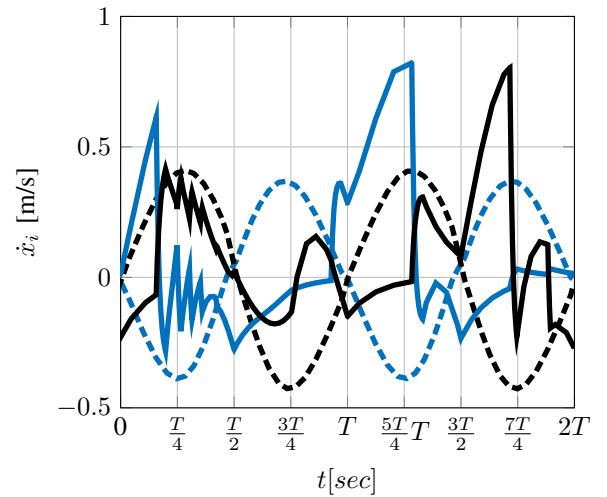


Fig. 14: Contacts' velocities of feedback control gait (solid curves) and prescribed-angles gait (dashed curves) for $\omega = 8$ [rad/s] – \dot{x}_1 (blue) and \dot{x}_2 (black)

An illustration of a gait with this control law, compared to the reference trajectories (in dashed curves) is given in Fig. 13 for control parameters $\mathbf{K}_v = 10\mathbf{I}$, $\mathbf{K}_P = 80\mathbf{I}$, $\mathbf{K}_D = 100\mathbf{I}$, $\Phi = [90^\circ, 130^\circ]$, and reference joints trajectories (5) with the parameters $\omega = 8$ [rad/s], $A = 18^\circ$, $\varphi_0 = 110^\circ$ and $\psi = 20^\circ$. Interestingly, the solution converges in steady state to a two-step periodic solution, with mean distance $S = 48.4$ [mm], compared to only 3.6 [mm] for the same joints trajectories without feedback. The difference is explained by comparing the the contacts' velocities with and without the feedback control in Fig. 14. Clearly, in this case the feedback control law significantly reduces the undesired opposing slippage, but such gaits were only found for a range of frequencies and careful tuneup of the control coefficients (as discussed in details in Section VIII, along with other limitations and requirements of this approach).